Journal of Inclusion Phenomena and Molecular Recognition in Chemistry **21**: 215–237, 1995.

Zeolite Guest-Host Interactions: Implications in Formation, Catalysis, and Photochemistry

PRABIR K. DUTTA

1. Introduction

Zeolites are crystalline aluminosilicates with the composition $M_{x/n}\cdot(AlO_2)_x\cdot(SiO_2)_y\cdot wH_2O$ [1]. The framework is formed by -Si-O-Al(Si)- bonds and about 75 different topologies comprising of cages and channels with varying molecular dimensions are known [2]. The intracrystalline zeolitic space is occupied by H_2O molecules which can be removed upon heating. The M^{n+} cations, which neutralize the charge carried by the tetrahedral framework aluminum, are readily exchangeable. The close match in size between reactant molecules and the zeolite interior has been extensively exploited in hydrocarbon transformations, leading to many novel processes [3]. Reactions showing selectivity towards specific reactants, formation of specific products, as well as novel control of the transition state and molecular traffic control due to different intrazeolitic diffusivities of reactants and products, have all been observed [4].

We have exploited the close size match between the zeolite interior and structure-directing molecules to provide information on the assembly process of zeolites. In addition, entrapment of organometallic molecules in zeolite Y supercages has allowed us to examine reactant selectivity in olefin oxidation, stabilization of dioxygen complexes, and partitioning of molecules for directional photochemical transfer. We have also developed Raman spectroscopy, in both its spontaneous and resonance enhanced forms, to examine encapsulation. This technique has provided information about the interactions between zeolite guest and host at the molecular level. The examples discussed in this paper will illuminate how encapsulation can be exploited to understand various aspects of zeolite formation as well as zeolite guest-host reactivity.

2. Entrapment as a Monitor for Zeolite Assembly

It is well known that organic molecules direct the transformation of aluminosilicate gels to distinct framework structures [5]. In many of these syntheses, the organic molecule becomes trapped within the zeolite framework. The exact role played by these molecules in directing zeolite formation is an area of current research [6]. Various studies have

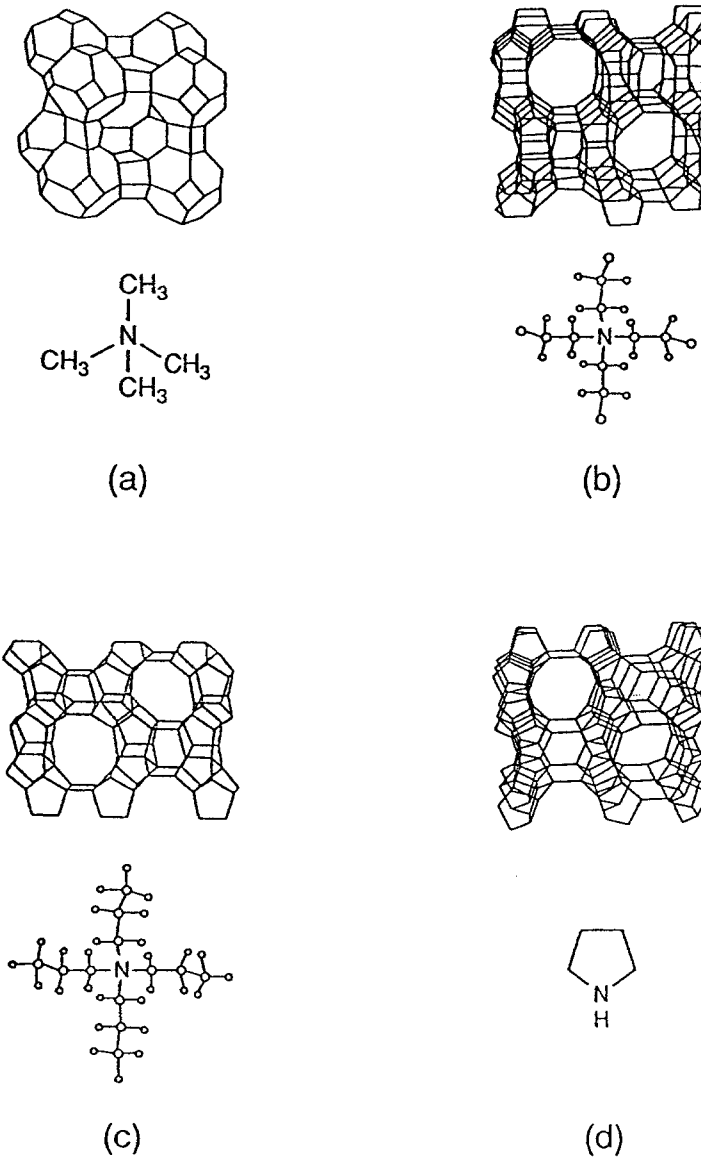

Figure 1. Structure of zeolitic frameworks and the corresponding structure directing agents: (a) TMA for ZK-4; (b) TEA for mordenite; (c) TPA for ZSM-5; and (d) pyrrolidine for ferrierite.

focused on the transformation of the inorganic aluminosilicate gel to zeolite, primarily by Raman [7-11] and solid state NMR spectroscopy [12-14]. Raman studies have shown that it is possible to detect four- and five-membered aluminosilicate rings in the gel [7-11], though how these units combine to form the long-range order inherent in these frameworks is not understood. Thus, what appears to be missing is information on the development of the porosity of these crystals. We have tried to address this shortcoming by focusing on the organic molecule as the organic-aluminosilicate system evolves towards a zeolitic framework. The strategy was to examine whether encapsulation of organic by the zeolite results in a strong enough perturbation to alter the characterization properties of the organic moiety. Information about zeolite assembly is then obtained by monitoring that structural perturbation. Raman spectroscopy is found to be particularly useful. Since the scattering cross-section of the organic moiety is considerably higher than the aluminosilicate framework, the Raman frequencies are a sensitive monitor of structural changes while the Raman scattering of water, the typical solvent in zeolite synthesis, has a small Raman scattering cross-section [15].

Figure 1 compares the structures of four structure-directing agents: tetramethylammonium ion (TMA), tetraethylammonium ion (TEA), tetrapropylammonium ion (TPA), and pyrrolidine (PL) and the zeolitic frameworks synthesized in the presence of these agents: zeolite A or ZK-4 (TMA) [16], mordenite (TEA) [17], ZSM-5 (TPA) [18], and ferrierite (PL) [19].

Figure 2 shows the Raman spectra of the structure-directing agents upon encapsulation into zeolites. Upon comparison with the spectra of the free structure-directing agents in solution, we have noted a number of spectral changes. These changes are highlighted as inserts in Figure 2 by showing the spectra of the unperturbed organic. Only in the case of TEA, which is responsible for the formation of mordenite, are no changes observed upon encapsulation, and thus no insert is shown.

By monitoring the Raman spectrum of the organic during zeolite growth, information about the entrapment and thereby the process of zeolite assembly and the development of porosity for three of these frameworks (ZK-4, ZSM-5, ferrierite) has been obtained. We will focus first on the results of the individual zeolite systems followed by a general discussion of zeolite assembly.

2.1 ZK-4 (ZEOLITE A FRAMEWORK)

The TMA cation results in synthesis of ZK-4, which has an architecture similar to that of zeolite A, but with Si/Al >1. As shown in Figure 1, there are two cages in ZK-4 which may contain the TMA ion, the α- or β-cages. The β-(sodalite)-cage has an internal dimension of ~6.4 Å, whereas the α-cage is ~8 Å. The dimension of the TMA cation is about ~6.4 Å. When positioned inside the α-cage [20], the Raman spectrum of TMA resembles that of the free-ion in solution. However, if it is held in the sodalite cage, the close match between the molecular size and the cage leads to a perturbation of the stretching frequencies: 752 cm^{-1} to 761 cm^{-1} for the C-N symmetric stretch and 950 to

955 cm^{-1} for the asymmetric C-N stretch [20,21]. This is evident from the Raman spectrum of TMA inside the zeolite sodalite where all of the TMA ions are entrapped in β-cages and is shown in Figure 3a.

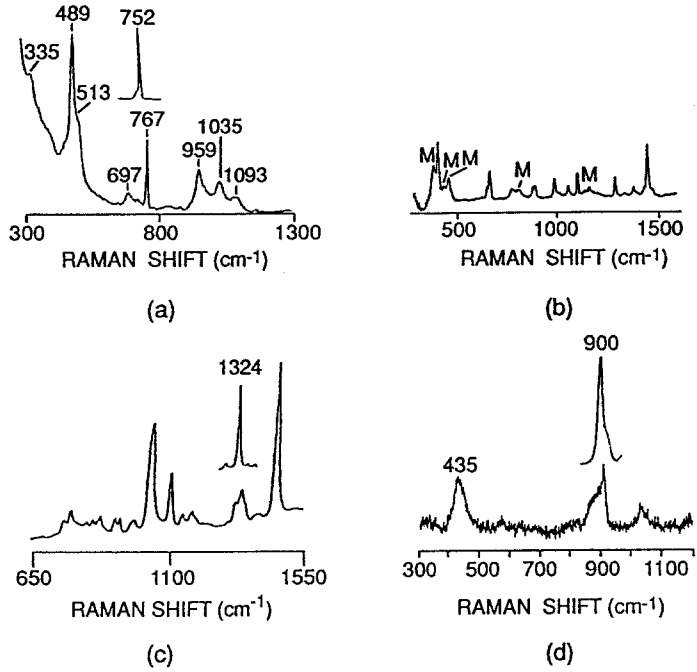

Figure 2. Raman spectra of structure-directing agents trapped in zeolite cages: (a) TMA in ZK-4; (b) TEA in mordenite; (c) TPA in ZSM-5; and (d) pyrrolidine in ferrierite. The insets on the figures show the spectrum of the structure-directing agent in solution.

The change in frequencies results from an increase in volume during the stretching vibrations which is met by resistance from the tightly surrounding cage framework and resembles the effect of increased pressure. Figure 3b represents this schematically. Therefore, these shifts in the Raman frequency of the TMA signal the formation of sodalite cages during the zeolite assembly process.

Figure 4 shows the Raman spectra of the aluminosilicate gel as a function of crystallization time for ZK-4. These spectra were obtained at room temperature from samples quenched at various times from the reaction mixture kept at 85° C [20].

The first appearance of the 767 cm^{-1} band (i.e., distinct sodalite cages) after 20 hours of synthesis coincided with the appearance of crystals as determined by X-ray diffraction experiments. This suggests that the formation of sodalite cages occurs with the assembly of the crystal itself. Thus, we conclude that the zeolite superstructure is not growing by assembly of the sodalite building units. Rather, the sodalite cages are formed concurrently with the zeolite superstructure of ZK-4.

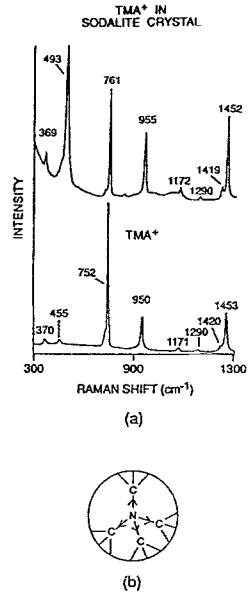

Figure 3. (a) Raman spectra of TMA in solution and in a sodalite crystal. (b) Symmetric stretching vibration of TMA entrapped in a sodalite cage (adapted from [20]).

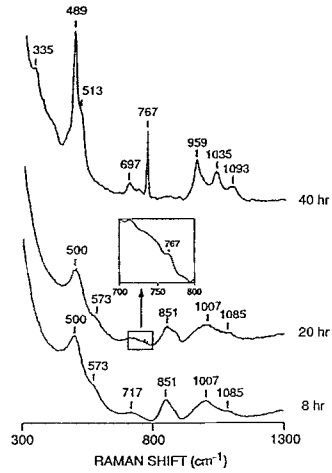

Figure 4. Raman spectra of the aluminosilicate gel during ZK-4 synthesis in the presence of TMA. The inset at 20 hour shows the first appearance of the entrapped TMA ion (adapted from [20]).

2.2 ZSM-5 (PENTASIL FRAMEWORK)

In the synthesis of ZSM-5, the vibrational changes of the TPA molecule highlighted in Figure 2 arise from a change in the geometry of the entrapped TPA cation. The TPA cation normally exists in its all *trans* form [22]. However, this geometry cannot be accommodated in the zig-zag intersecting channels of ZSM-5. A rotation around the C-C bond is required, as shown in Figure 5 [23].

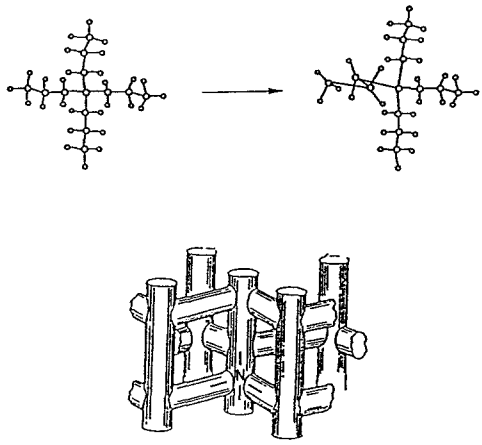

Figure 5. Conformational change of the TPA ion required to fit into the zig-zag channels of ZSM-5.

This results in splitting of the CH_2 wagging mode into two bands at 1324 and 1343 cm^{-1}. Thus, appearance of this band splitting during zeolite growth indicates the formation of the zig-zag chains of the ZSM-5 superstructure [22]. Figure 6 shows the Raman spectral evolution of the gel phase as a function of heating time.

Entrapment of the TPA ion is observed at the earliest stages of synthesis after one day of heating. Crystal formation is observed after four days of heating, as determined by X-ray diffraction. However, it is interesting to note that encapsulation at the earliest stages (< 2 days) leaves the TPA in its all *trans* form, i.e., no zig-zag chains are formed. It is only after three days of synthesis that the C_2-C_3 rotated conformer of TPA is observed, indicating the first formation of zig-zag chains and the superstructure of ZSM-5. Immediately following this, the crystals of ZSM-5 are observed in the diffraction experiments. There is a similarity between this system and that of the previously discussed ZK-4 in that the cage superstructure is formed at the end of the assembly process. Thus, crystal growth is not occurring by assembly of units consisting of trapped TPA ions at the intersection of channels, but rather the zig-zag chains are forming at the final stages of zeolite assembly.

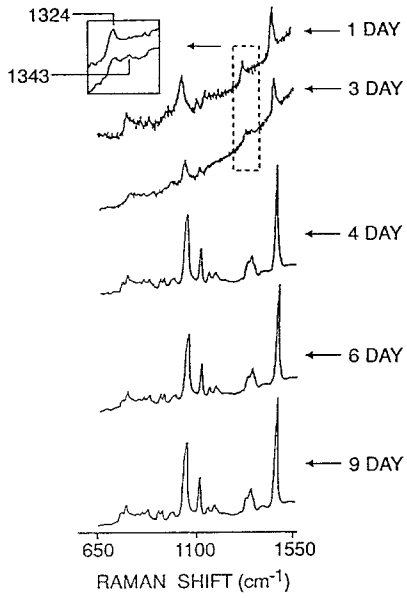

Figure 6. Raman spectra of the aluminosilcate gel during synthesis of ZSM-5 in the presence of TPA (adapted from [23]).

2.3 FERRIERITE FRAMEWORK

The above view of zeolite formation is also supported by the observations of the role of pyrrolidine in the synthesis of ferrierite [24]. Figure 7 shows the Raman spectral evolution of the gel as a function of synthesis time.

The earliest change observed, after 11 hours of heating, is the splitting of the 900 cm^{-1} band, which occurs as a result of protonation of the amine nitrogen and is assigned to the NH_2 wagging mode [25].

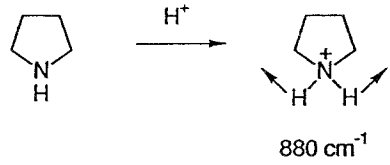

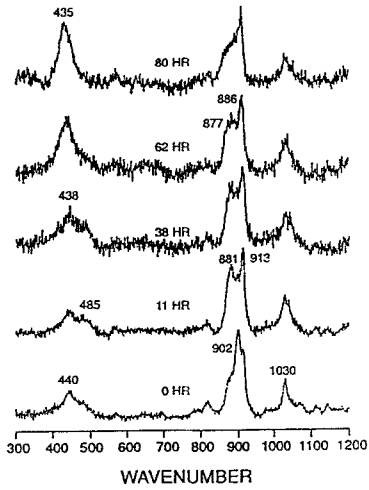

Figure 7. Raman spectra of aluminosilicate gel during synthesis of ferrierite in the presence of pyrrolidine (adapted from [24]).

This indicates that, at the early stages, the pyrrolidinium ion is being formed and is present in the aluminosilicate gel, the NH_2^+ group neutralizing the charge on the aluminum. The evolution of this wagging mode as a function of synthesis is of importance. It splits into several bands and then, at the final stage of crystallization, appears as a broad band. Since the broad band at 880 cm^{-1} evolves from a single band through intermediate stages of split bands, we have assigned these as due to the pyrrolidinium cation being in slightly different environments, with different $NH_2^+ \cdots O$ hydrogen bonds with the aluminosilicate framework [24]. We have interpreted these changes as progressive entrapment of the pyrrolidinium ion as the zeolite superstructure forms.

2.4 THE ASSEMBLY PROCESS

These observations point to an evolution of zeolite assembly in which the primary overall structure is formed first followed by a gradual increase in local ordering. Thus, complete entrapment of the organic does not appear in the initial step in nucleation, but rather occurs in the final stages.

Within the scope of the above studies and other studies in the literature, the role of the entrapped organic in zeolite synthesis occurs at several levels:

(a) The organic can modify the gel chemistry, e.g., it is well known that TMA stabilizes 4-membered aluminosilicate rings, whereas TPA does so for

5-membered rings [26,27]. We have shown that pyrrolidine stabilizes gels containing 5-membered rings [24].

(b) The organic needs to associate strongly with the aluminosilicate gel, as we have noted above. This is done through electrostatic, hydrophobic, and H-bonding interactions.

(c) Entrapment results at the final stages of zeolite assembly.

These observations are outlined schematically in Figure 8 as a model of zeolite synthesis.

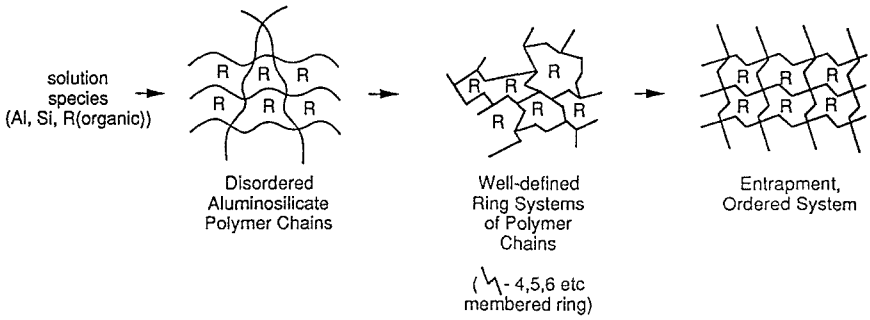

Figure 8. A schematic model of zeolite assembly.

3. Entrapment of Organometallic Complexes in Zeolite Y Cages

Organometallic complexes exhibit an unusually rich chemistry involving catalysis, ligand binding, and photochemistry in homogeneous solution, in biological systems, and on supports [28-29]. The cages of zeolites provide a unique host for these molecules, since they can be isolated from each other and the external world, yet can interact with reactants that penetrate through the ring system of the zeolite. Our primary emphasis has been on the large cages of zeolites A and Y as hosts. In section 2.1, we discussed the structure of zeolite A. A schematic of the zeolite Y supercage is shown in Figure 9. These super cages have dimensions of ~13 Å with openings of ~7 Å.

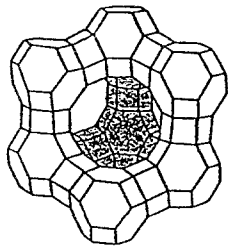

Figure 9. A zeolite Y supercage.

Complexes entrapped in these cages then have access to the external environment through the ~7 Å windows. Below we present our results on examining the interactions of the entrapped complexes in zeolite cages with reactants varying widely in size from aromatic olefins to dioxygen to photochemically generated electrons.

3.1 OLEFIN OXIDATION

Several studies have been reported on the oxidative ability of manganese, chromium, and nickel complexes of SALEN [SALEN = N,N'-ethylene-bis-salicylidene-aminato] in homo-geneous systems [30]. This ligand system is attractive from an encapsulation point of view, since it forms metal complexes of dimensions 10-11 Å, that can be trapped in the zeolite Y supercages. Our focus was on Mn^{III}SALEN-Y and its catalytic activity towards various olefins [31]. Iodosylbenzene (PhIO) was chosen to be the terminal oxidant:

$$\text{olefin} + \text{PhIO} \xrightarrow[\text{zeolite catalyst}]{} \text{products} + \text{PhI}$$

Table I shows the reactivity for a range of olefins that we have examined. The olefins are listed in order of increasing size: cyclohexene, 6.7 x 7.4 Å; styrene, 6.7 x 9.5 Å; *trans*-stilbene, 6.7 x 13.9 Å; and *cis*-stilbene, 8.0 x 10.3 Å.

In the case of cyclohexene, the amount of olefin that reacted is comparable to the PhI formed. The products were cyclohexene oxide and cyclohexenol, as identified by GC.

Table I. Olefin oxidation by MnSALEN-Y.

Olefin	olefin reacted (mmol)	PhI formed* (mmol)	Ratio (olefin/PhI)	Product mmol (%)
Cyclohexene	0.11	0.11	1	0.015 (14) cyclohexene oxide; 0.011 (10) cyclohexenol
Styrene	0.057	0.092	0.6	0.011 (19) styrene oxide; 0.015(26) $PhCH_2CHO$
Trans-stilbene	0.048	0.090	0.5	0.01(20) *trans*-stilbene oxide
Cis-stilbene	0.019	0.085	0.02	*cis*-stilbene oxide

* 0.11 mole of PhIO used.

For styrene and the stilbenes, the PhIO consumed is considerably greater than the olefin reacted. We have proposed that the solvent molecules (acetonitrile) are undergoing oxidation [31]. The competition with solvent oxidation increases as the olefins get larger and the diffusivity within the zeolite system becomes more difficult. The lower diffusivities of the larger olefins, however, leads to a reversal of the relative reactivities, as compared to homogeneous solutions, thus exhibiting size selectivity. With the zeolitic catalyst, cyclohexene is twice as reactive as styrene and three times as reactive as *trans*-stilbene. In the homogeneous system, the opposite trend, with *trans*-stilbene being one and a half times more reactive than cyclohexene, was found [30]. In the homogeneous system, too, oxidation of the solvent is a problem but it is not as severe as with the zeolite. This is because in homogeneous solution the reaction is complete within 30 minutes, but in the zeolite it takes over 16 hours. The MnSALEN-zeolite Y complex exhibited catalytic activity for over 60 hours; the long term stability presumably arising due to encapsulation.

What this study showed is that catalysts from homogeneous systems can indeed be transposed into the cages of zeolites and still promote the olefin oxidation reactions observed in solution. The zeolitic system also shows reversal of reactivity as compared to homogeneous solution because of restrictions in diffusivity. However, the problem is that the lower diffusivities lead to considerably lower rates of reactions. This may not have been a problem in itself, but becomes so because the catalyst is active enough to oxidize the solvent. Since the solvent molecules are considerably smaller than the substrates and are present at much higher concentrations, this competition detracts from the overall usefulness of the system.

3.2 DIOXYGEN BINDING

It is clear from the system discussed above that encapsulation in zeolite cavities allows for the isolation of metal complexes. This strategy has been used in the literature to stabilize complexes which in solution will dimerize and thereby deactivate [32-34]. Excellent examples are the O_2 dioxygen complexes of transition metals. It is well known that many low-spin Co^{II}-ligand complexes will bind O_2, but then rapidly dimerize to form peroxo complexes. By building the complex in a zeolite cage with a sufficiently large ligand, only a monomeric form can be accommodated. Herron has explored this with a CoSALEN complex using pyridine as the axial base [32]. Lunsford et al. have synthesized bipyridine and terpyridine complexes of Ru that also bind dioxygen [33].

We chose to synthesize dioxygen complexes using tetraethylenepentamine (tetren) as ligand (shown below) [35]. There were two advantages we saw with this ligand. Firstly, it is a pentadentate ligand, thus eliminating the need for an axial base. Secondly, it is soluble in water, thus allowing for ready transport into the zeolite pores. We examined both zeolite Y and A as supports, the cage diameters being ~13 and ~11.4 Å, respectively.

$NH(CH_2CH_2NHCH_2CH_2NH_2)_2$

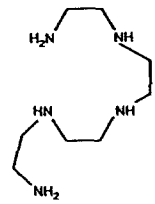

Resonance Raman spectra of the Co(tetren)-dioxygen complex in the cages of zeolites Y and A are shown in Figure 10 [35]. In the case of zeolite Y, the bands at 498, 643, and 808 cm^{-1} are readily assigned to Co-N, Co- O, and the O-O stretch of the peroxo complex [36]. In the case of zeolite A, new bands are observed at 580, 1034, and 1138 cm^{-1}. The bands at 580 and 1138 cm^{-1} are characteristic of the Co-O and O-O stretching modes of superoxo complexes [37].

Thus, the chemistry can be summarized as:

Zeolite Y: $2Co(tetren) + O_2 \rightarrow$ (tetren) Co-O-O-Co(tetren)

Zeolite A: $Co(tetren) + O_2 \rightarrow$ (tetren) $Co\text{-}O_2$.

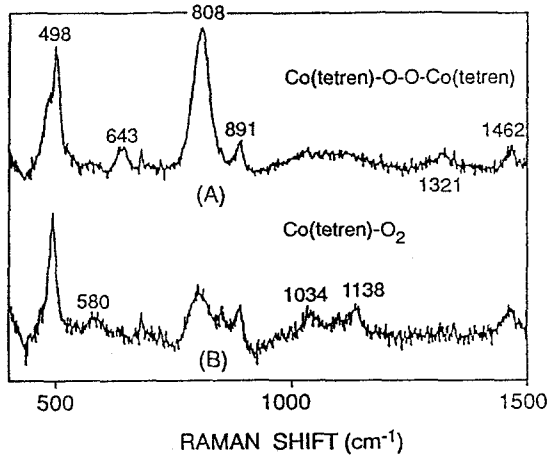

Figure 10. Resonance Raman spectra of Co(tetren)-O_2 complex in zeolites A and Y (adapted from [35]).

There is some peroxo complex also in the zeolite A sample. Modeling of the size of the Co(tetren) shows it to be between 7-8 Å. This means that the complex can exist as a dimer in zeolite Y supercages (~13 Å) but can exist only as a monomer in a zeolite A α-cage (~11.4 Å). The observation of a peroxo complex with the zeolite A sample probably arises from dimers formed on the outside surface of the zeolite crystallites, an observation not atypical for synthesis in aqueous solution [37].

EPR spectra of the complexes formed in zeolites Y and A support the Raman characterization and are shown in Figure 11. The complex in zeolite Y exhibits a very weak signal, probably arising from iron impurities in the zeolite. The μ-peroxo dimer is not expected to produce an EPR signal since the electrons are paired on

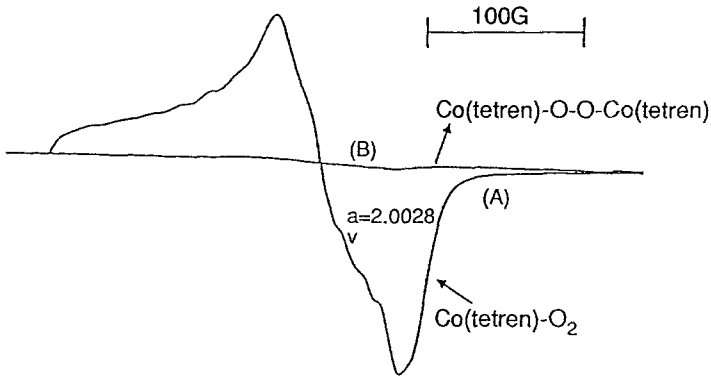

Figure 11. EPR spectra of Co(tetren)-O_2 complex in (A) zeolite A and (B) zeolite Y (adapted from [35]).

the Co-O-O-Co unit. The EPR spectrum from the complex in zeolite A is typical of a Co^{III}-O_2^- superoxo complex, with the hyperfine splitting expected due to the Co($I=^7/_2$) nucleus [38].

It is possible to remove the O_2 from the Co(tetren)-O_2 complex in zeolite A by exposing it to N_2. The complex can be re-formed after re-exposure to O_2. This cycle is captured by the EPR spectra shown in Figure 12. The binding constant was estimated to be 2.2 x 10^3 M^{-1}, indicating that Co(tetren) binds O_2 very strongly.

Thus, this study showed that zeolite encapsulation leads to the stabilization of complexes not easily obtained in aqueous solution. Since O_2 is a much smaller reactant than the previously discussed olefins, its diffusivity into the zeolite was not a problem. The drawback in this case (from an application point of view for separating O_2 from N_2) was that, the binding of O_2 to Co(tetren) in zeolite A was very tight and reversed only with difficulty. This notwithstanding, it is clear that the close fit between interesting molecular systems and the zeolite cages allows for assembly of novel chemical systems.

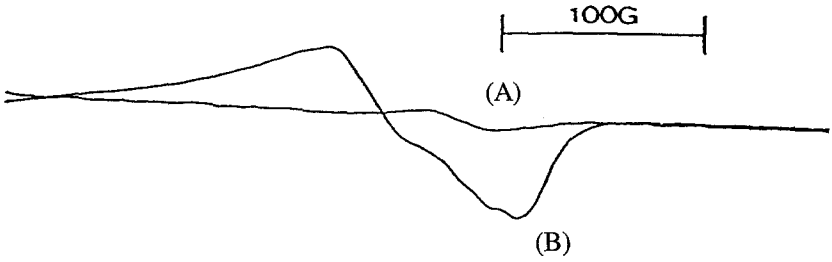

Figure 12. EPR spectra of Co(tetren)-O_2 complex (A) upon exposure to N_2 and (B) re-exposure to O_2 (adapted from [35]).

3.3 PHOTOCHEMICAL CHARGE SEPARATION

There is considerable interest in developing systems that can convert sunlight to chemical energy. In particular, if such schemes can result in conversion of readily available chemicals to fuels, it makes this chemistry particularly important [39].

$$2H_2O \rightarrow 2H_2 + O_2 \qquad \Delta G = \quad 68.3 \text{ kcal/mole}$$

$$2H_2O + CO_2 \rightarrow CH_4 + 2O_2 \qquad \Delta G = \quad 195.5 \text{ kcal/mole}$$

In both these examples, the uphill free energy can, in principle, be provided by solar energy. The processes also involve transfer of electrons, i.e., they are redox reactions. Attempts to use light energy for these reactions can exploit photochemical electron-transfer [40], as in:

$$D \xrightarrow{h\nu} D^*$$

$$D^* + A \rightarrow D^+ + A^-$$

$$4D^+ + 4OH^- \rightarrow O_2 + 4D + 2H_2O$$

$$2A^- + 2H^+ \rightarrow H_2 + 2A$$

where D is the molecular species that absorbs the light and has a long-lived excited state (D^*). In this excited form, it can donate an electron to an acceptor molecule, A. If D and A are chosen appropriately, then D^+ and A^- can bring about redox chemistry, such as shown above, in splitting of H_2O into H_2 and O_2. Since D and A are regenerated, the process can be made cyclic. However, the difficulty which needs to be circumvented in order for this strategy to work is to separate D^+ and A^- after they are formed, since there is a strong driving force for the back-electron-transfer reaction. The best example of such a system is found in photosynthesis, in which a membrane is used as a host for a complex arrangement of acceptors and donors, designed optimally for charge separation [41].

We have investigated the possibility of using the cages of zeolites as a partitioning medium for entrapping D and A in order to enhance photochemical charge separation. Our choice of D and A were $Ru(bpy)_3^{2+}$ and bipyridinium cations (viologens) for several reasons.

$$Ru(bpy)_3^{2+} \rightarrow Ru(bpy)_3^{2+*}$$

$$Ru(bpy)_3^{2+*} + MV^{2+} \rightarrow Ru(bpy)_3^{3+} + MV^{+\bullet}$$

Firstly, this system has been extensively examined in aqueous solutions [42]. Secondly, the D^+ and A^- forms have the requirements to convert H_2O to O_2 and H_2, respectively [43]. Thirdly, these molecules satisfy the architectural requirements for assembly within the zeolitic system, as explained below.

Figure 13a shows the results of photolysis with visible light (420-650 nm) of an aqueous solution of 0.1 M $Ru(bpy)_3^{2+}$ and 0.01 M methylviologen (MV^{2+} = $CH_3N^+C_5H_4\ C_5H_4N^+CH_3$) as measured by the electronic spectra. The band at 450 nm due to the MLCT band of $Ru(bpy)_3^{2+}$ remains unperturbed and no evidence of any electron transfer is detected. Figure 13b shows the same system with triethanolamine added. Within seconds of photolysis, bands at 390 and 610 nm due to the radical cation of methylviologen ($MV^{+\bullet}$) are observed. The chemistry is as follows:

$$Ru(bpy)_3^{2+} \xrightarrow[h\nu]{450nm} Ru(bpy)_3^{2+*}$$

$$Ru(bpy)_3^{2+*} + MV^{2+} \rightleftarrows Ru(bpy)_3^{3+} + MV^{+\bullet}$$

$$Ru(bpy)_3^{3+} + N(CH_2OH)_3 \rightarrow Ru(bpy)_3^{2+} + \text{degradation products}$$

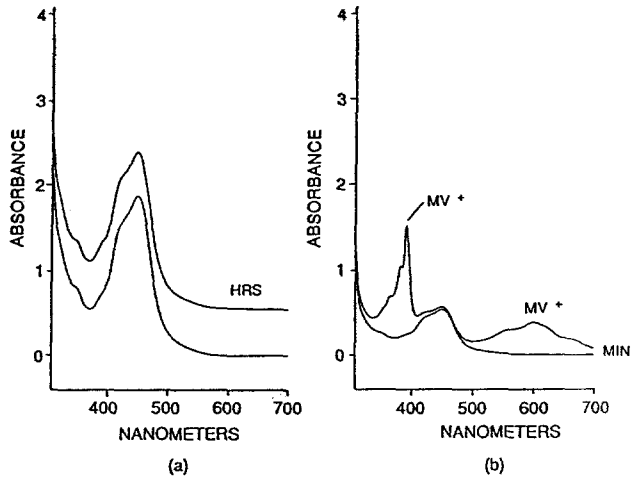

Figure 13. Visible light photolysis of $Ru(bpy)_3^{2+}$ and MV^{2+} in (a) an aqueous solution and b) in the presence of triethanolamine.

In the presence of the sacrificial electron donor, triethanolamine, a fraction of the $Ru(bpy)_3^{3+}$ reacts with it before the back-electron-transfer reaction can occur, thus stabilizing the $MV^{+\bullet}$ [44]. The absence of any $MV^{+\bullet}$ in Figure 13a is due to the rapid back-electron-transfer reaction.

The zeolite offers a novel way to arrange the $Ru(bpy)_3^{2+}$ and MV^{2+}. $Ru(bpy)_3^{2+}$ is a molecule of ~13 Å dimension and, if synthesized inside a zeolite supercage, is entrapped since it cannot escape through the ~7 Å openings [45-47]. However, it can still communicate with molecules in neighboring cages through the 7 Å windows. This complex can readily be synthesized in situ within the zeolite supercage by heating bipyridine with $Ru(NH_3)_6^{3+}$-exchanged zeolite Y, as shown below.

$$\text{Na-Y} + \text{Ru}(\text{NH}_3)_6^{3+} \xrightarrow{\text{ION-EXCHANGE}} \text{Na,Ru}(\text{NH}_3)_6^{3+}\text{-Y}$$

$$\text{Na,Ru}(\text{NH}_3)_6^{3+}\text{-Y} + 3\ \text{bpy} \xrightarrow{\text{HEAT}} \text{Na,Ru}(\text{bpy})_3^{2+}\text{-Y}$$

95% YIELD

$$Na,Ru(bpy)_3^{2+}\text{-}Y \xrightarrow[\text{EXCHANGE}]{\text{SOXHLET NaCl}} \text{PURIFIED SAMPLE}$$

The initial loading level of $Ru(NH_3)_6^{3+}$ determines how closely the Ru units are packed. This can vary from very dilute loadings, i.e., 1 Ru per 1000 supercages, to a maximum of 1 Ru per cage [48]. In the studies discussed in this paper, the packing is about 1 $Ru(bpy)_3^{2+}$ per 10-15 supercages.

The MV^{2+} cations can readily be ion-exchanged into the Na-$Ru(bpy)_3^{2+}$-Y from aqueous solution to a maximum loading of 2 MV^{2+} per supercage [49]. The dimensions of this molecule are ~13 x 6 Å, so it travels readily through the ~7 Å openings [50]. However, MV^{2+} is not likely to be in the supercages occupied by $Ru(bpy)_3^{2+}$, since this complex completely fills the supercage. Thus, a $Ru(bpy)_3^{2+}$,MV^{2+} - zeolite sample has the $Ru(bpy)_3^{2+}$ partitioned in a supercage and surrounded by MV^{2+} in the neighboring cages separated by the ~7 Å windows.

In order to establish that electron-transfer can occur upon photoexcitation in this architecture, we examined the time-resolved resonance Raman spectrum of the sample [51]. The 20 ns, 366 nm photon excites the $Ru(bpy)_3^{2+}$ and also serves as the excitation for the Raman spectrum. As Figure 14 shows, within the 20 ns pulse, we observe the spectrum characteristic of the $MV^{+\bullet}$ radical with bands at 1360, 1535, and 1661 cm^{-1} [52]. This is evidence for oxidative quenching through the 7 Å windows.

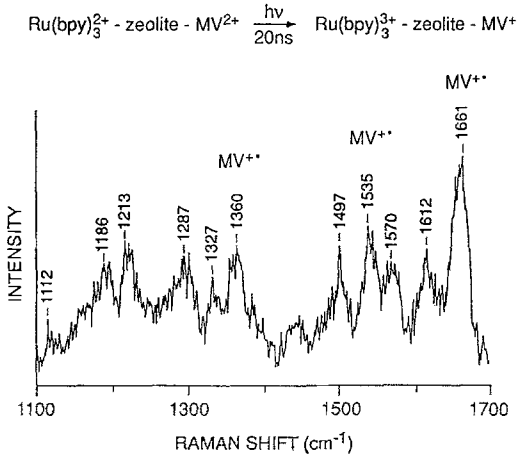

Figure 14. Time-resolved resonance Raman spectrum of $Ru(bpy)_3^{2+}$,MV^{2+}-Y (adapted from [51]).

Time-resolved diffuse reflectance spectra show that the $MV^{+\bullet}$ radical-cation formed, decays back with a half-life of 10 μsec and follows second-order kinetics as expected for the bimolecular back-electron-transfer reaction [51].

However, continuous photolysis (450-620 nm) showed that the radical cation ($MV^{+\bullet}$) can be stabilized, even though its rate of formation is very slow. Figure 15 shows the diffuse reflectance spectra as a function of photolysis time, and the bands due to $MV^{+\bullet}$ at 390 and 610 nm are found to grow. Upon turning off the light, the $MV^{+\bullet}$ decays back in tens of minutes [51].

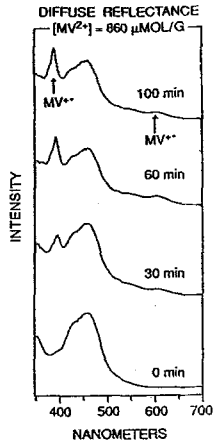

Figure 15. Diffuse reflectance spectra of $Ru(bpy)_3^{2+}$,MV^{2+}-Y as a function of photolysis time (420-650 nm).

A mechanistic scheme consistent with these observations is shown below.

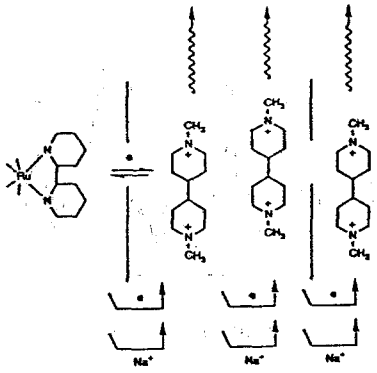

It is emphasized that upon oxidative quenching, the back-electron-transfer is the dominant reaction. However, there is another low efficiency pathway, in which the optimal packing of the viologen molecules leads to electron-hopping and charge separation. This process is facilitated in the zeolite by the migration of co-cations (i.e., Na^+) along with electron movement. Once the charge is separated in this fashion, the back-electron transfer is considerably slowed down.

The problem in this design is that most of the time the oxidative quenching is followed by the back-electron-transfer reaction. Clearly, a more efficient route is required. In order to do so, we have focused our attention on a ternary system, thus providing a pathway for a subsequent electron transfer step after the primary oxidative quenching [53]. This strategy is illustrated below schematically in Figure 16.

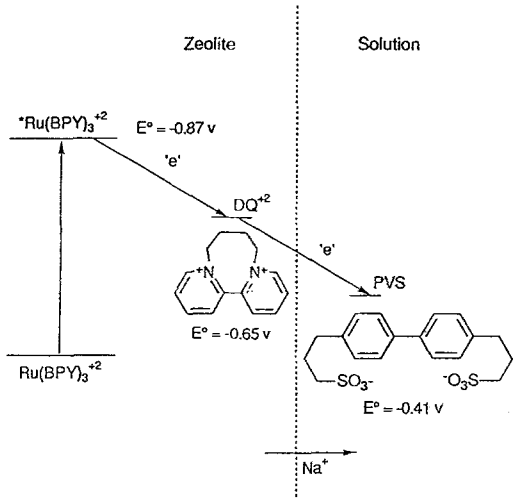

Figure 16. A strategy for efficient photochemical charge-transfer using zeolitic architecture.

In order to provide a directional push for electron-transfer, we chose two viologens with different reduction potentials. The viologen with the higher redox potential (DQ^{2+}, E_0 = -0.65 V) [54] was ion-exchanged into the zeolite and surrounded the entrapped $Ru(bpy)_3{}^{2+}$. A neutral viologen (PVS) with a lower reduction potential (E_0 = 0.41 V) [54] was introduced into the external aqueous medium. By choosing it to be a neutral species, there was no possibility of the PVS replacing the DQ^{2+} in the zeolite. The extent of photochemical charge separation was readily analyzed by monitoring the PVS radical formed in solution. Figure 17 compares the yield of radical as a function of time for the $Na,Ru(bpy)_3{}^{2+}$-Y and $Ru(bpy)_3{}^{2+},DQ^{2+}$-Y with PVS in solution. There is a marked

increase in the yield of the radical in the ternary system. If the intrazeolitic DQ^{2+} is replaced with MV^{2+}, whose reduction potential (-0.44 mV) is comparable to that of PVS, then the yield of radical drops again to that of the binary system, indicating that the strategy of vectorial electron-transfer is necessary.

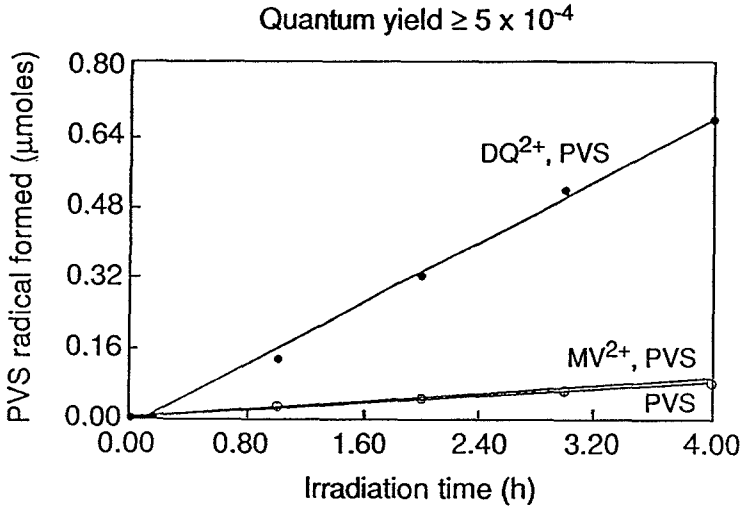

Figure 17. Yield of the PVS radical in solution as a function of photolysis time in the ternary system.

There are several aspects of the zeolite architecture that have been exploited in order to achieve this efficient charge separation. Firstly, the supercages isolate the $Ru(bpy)_3^{2+}$ molecule. Secondly, the ion-exchanging ability of the zeolite is used to hold the charged viologens in place around the $Ru(bpy)_3^{2+}$ sensitizer. Thirdly, the negative charge of the framework helps in repelling the PVS radical after interfacial electron-transfer, promoting charge separation. Fourthly, along with the injection of the electron into PVS in solution, a charge neutralizing Na^+ is also injected into solution, thus maintaining neutrality and preventing an opposing junction potential.

In summary, the purpose of this review, based primarily on the work done by our group has been to show that the close fit in size between zeolite cages and molecules can be exploited to derive information about zeolite assembly, as well as, assembling superstructures that allow for novel chemical and photochemical applications.

Acknowledgments

I would like to thank all my students and colleagues, whose names appear in the manuscripts. In addition, thanks are also due to the National Science Foundation and Department of Energy for financial support.

References

1. D. W. Breck, *Zeolite Molecular Sieves*, Krieger Publishing, Malabar, Florida (1984).
2. J. M. Newsam, *Science*, **231**, 1093 (1986).
3. J. W. Ward, *Applied Industrial Catalysis*, **3**, 271 (1984).
4. S. Csicsery, *Zeolites*, **4**, 202 (1984).
5. B. M. Lok, T.R. Cannan, and C.A. Messina, *Zeolites*, **3**, 282 (1983);
   R.M. Barrer, *Hydrothermal Chemistry of Zeolites*, Academic Press, London (1982).
6. M. E. Davis and R. F. Lobo, *Chem. Mater.*, **4**, 756 (1992).
7. P. K. Dutta and D. C. Shieh, *J. Phys. Chem.*, **90**, 2331 (1986).
8. P. K. Dutta, D. C. Shieh, and M. Puri, *J. Phys. Chem.*, **91**, 2332 (1987).
9. P. K. Dutta, D. C. Shieh, and M. Puri, *Zeolites*, **8**, 306 (1988).
10. P. K. Dutta, M. Puri, and D.C. Shieh, *Mater. Res. Soc. Symp. Proc.*, **111**, 101 (1988).
11. P. K. Dutta, K. M. Rao, and J. Y. Park, *J. Phys. Chem.*, **95**, 6654 (1991).
12. A. V. McCormick and A. T. Bell, *Catal. Rev. Ser. Eng.*, **31**, 97 (1988).
13. P. Bodart, J. B. Nagy, Z. Gabelica, and E. G. Derouane, *J. Chim. Phys.*, **83**, 777 (1986).
14. C. D. Chang and A. T. Bell, *Catal. Lett.*, **8**, 305 (1991).
15. D. A. Long, *Raman Spectroscopy*, McGraw-Hill, NY (1977);
    D. Lin-Vien, N. B. Colthup, W. G. Fateley and J. G. Grasselli, *Infrared and Raman Characteristic Frequencies of Organic Compounds*, Academic Press, NY (1991).
16. H. Kacirek and H. Lechert, *ACS Symp. Ser.*, **40**, 244 (1977).
17. P. A. Jacobs and J. A. Martens, *Synthesis of High-Silica Aluminosilicate Zeolites*, Elsevier, Amsterdam (1987);
    S. Ueda, H. Murata, and M. Koizumi, *Am. Mineral.*, **65**, 1012 (1980);
    E. N. Givens, C. J. Plank, and E. J. Rosinski, *U. S. Patent* 4,052,472, (1972).
18. G. T. Kokotailo, D. H. Olson, S. L. Lawton, and W. M. Meier, *Nature (London)*, **272**, 437 (1978).
19. A. Araya and B. M. Lowe, *J. Chem. Res.*, **192**, (1985).
20. P. K. Dutta, B. DelBarco, and D. C. Shieh, *Chem. Phys. Lett.*, **127**, 200 (1986).
21. B. D. McNicol, G. T. Pott, K. R. Loos, and N. Mulder, *Adv. Chem. Ser.*, **121**, 152 (1973).
22. A. Zalkin, *Acta Crystallogr.*, **10**, 557 (1957).
23. P. K. Dutta and M. Puri, *J. Phys. Chem.*, **91**, 4329 (1987).
24. P. K. Dutta, K. M. Rao, and J. Y. Park, *Langmuir*, **8**, 722 (1992).
25. D. Garfinkel, *J. Am. Chem. Soc.*, **80**, 3827 (1958).
26. D. Hoebbel and W. Weiker, *Z. Anorg. Allg. Chem.*, **384**, 43 (1971).
27. E. J. J. Groenen, A. G. T. G. Korbeek, M. Mackay, and O. Sudmeijer, *Zeolites*, **6**, 403 (1986).

28. J. M. Thomas and K. I. Zamarev, *Perspectives in Catalysis*, Blackwell, Oxford (1992).
29. J. K. Kochi, *Organometallic Mechanisms and Catalysis*, Academic Press, NY (1978).
30. K. Srinivasan, P. Michaud and J. K. Kochi, *J. Amer. Chem. Soc.*, **108**, 2309 (1986); B. Muenier, E. Guilnet, M. DeCarvalho, and R. Poliblanc, *J. Am. Chem. Soc.*, **106**, 6668 (1984).
31. C. Bowers and P.K. Dutta, *J. Catal.*, **122**, 271 (1990).
32. N. Herron, *Inorg. Chem.*, **25**, 4714 (1986).
33. S. Imamura and J. H. Lunsford, *Langmuir*, **1**, 326 (1985).
34. G. Meyer, D. Worhle, M. Mohl, and G. Schulz-Ekloff, *Zeolites*, **4**, 30 (1984).
35. P. K. Dutta and C. Bowers, *Langmuir*, **7**, 937 (1991).
36. T. Shibahara and M. Mari, *Bull. Chem. Soc. Jpn.*, **51**, 1374 (1978).
37. K. Nakamoto, Y. Nanaka, T. Ishiguro, M. W. Urbana, M. Suzuki, M. Kozuka, Y. Nishida, and S. Kida, *J. Am. Chem. Soc.*, **104**, 3386 (1982).
38. R. J. Taylor, R. S. Drago, and J. E. George, *J. Am. Chem. Soc.*, **111**, 6610 (1989).
39. V. N. Parmev and K. I. Zamarev, in *Photocatalysis-Fundamentals and Applications*, N. Serpone and E. Pelizzetti (Eds.), John Wiley, N.Y., p 656 (1989).
40. K. Kalyansundaram, *Photochemistry in Microheterogeneous Systems*, Academic Press, NY (1987).
41. *Energy Conversion by Plants and Bacteria*, (Ed) Govindjee, Academic Press, NY (1982).
42. J. Olensted III and T. J. Meyer, *J. Phys. Chem.*, **91**, 1649 (1987); K. Mandal and M. Z. Hoffman, *J. Phys. Chem.*, **88**, 5632 (1984); M. Z. Hoffman, *J. Phys. Chem.*, **92**, 3458 (1988); C. Chiorleoli, M. T. Indelli, M. A. R. Scandola, and F. Scandola, *J. Phys. Chem.*, **92**, 156 (1988).
43. K. Kalyanasundaram, M. Gratzel, and E. Pelizzeti, *Coord. Chem. Rev.*, **69**, 57 (1986); J. M. Lehn, J. P. Sauvage, and R. Ziessel, *Nouv. J. Chim.*, **3**, 423 (1979); P. K. Ghosh, B. S. Brunschwig, M. Chou, C. Creutz, and N. Sutin, *J. Am. Chem. Soc.*, **106**, 4772 (1984).
44. G. Neshvad and M. Z. Hoffman, *J. Phys. Chem.*, **93**, 2445 (1989).
45. W. H. Quyale and J. H. Lunsford, *Inorg. Chem.*, **21**, 97 (1982).
46. J. A. Incavo and P. K. Dutta, *J. Phys. Chem.*, **94**, 3075 (1990).
47. K. Maruszewski, D. P. Strommen, K. Handrich, and J. R. Kincaid, *Inorg. Chem.*, **30**, 4579 (1991).
48. W. Turbeville, D. S. Robins, and P. K. Dutta, *J. Phys. Chem.*, **96**, 5024 (1992).
49. E. S. Brigham, P. T. Snowden, Y. I. Kim, and T. E. Mallouk, *J. Phys. Chem.*, **97**, 8650 (1993).
50. L. A. Summers, *The Bipyridinium Herbicides*, Academic Press, NY (1980).
51. P. K. Dutta and W. Turbeville, *J. Phys. Chem.*, **96**, 9410 (1992).

52. M. Forster, R. B. Girling, and R. E. Hester, *J. Raman Spectrosc.*, **12**, 36 (1982).
53. M. Borja and P. K. Dutta, *Nature*, **362**, 43 (1993).
54. I. Willner, A. Ayalon, and M. Rabinovitz, *Nouv. J. Chem.*, **14**, 685 (1990).

Abstract. This review primarily focuses on contributions of our research group in the area of zeolite guest-host chemistry. The perturbation of the Raman spectra of the organic structure-directing-agents during synthesis of zeolites ZK-4, ZSM-5, and ferrierite show clearly the entrapment of the organic by the aluminosilicate framework. The microordering around the organic coincides with the development of long-range-order typical of crystal formation. Using three examples involving zeolite entrapped organometallic complexes of manganese(III), cobalt(II), and ruthenium(II), we have demonstrated a wide range of chemistries using reactants varying from olefins to dioxygen to photogenerated electrons.